The effect of ambient pressure on laser-induced silicon plasma temperature, density and morphology

Cowpe, JS, Pilkington, RD, Astin, JS and Hill, AE

http://dx.doi.org/10.1088/0022-3727/42/16/165202

The effect of ambient pressure on laser-induced silicon plasma temperature, density and morphology.

J S Cowpe, R D Pilkington, J S Astin, A E Hill
Institute for Materials Research, Newton building Room 167, University of Salford, The Crescent, Salford, M5 4WT, UK

E-mail: j.s.cowpe@salford.ac.uk
E-mail: r.d.pilkington@salford.ac.uk
E-mail: j.s.astin@salford.ac.uk
E-mail: a.e.hill@salford.ac.uk

Abstract. Laser-Induced Breakdown Spectroscopy (LIBS) of silicon was performed using a nanosecond pulsed frequency doubled Nd:YAG (532 nm) laser. The temporal evolution of the laser ablation plumes was characterized under a range of low pressures. Electron densities were determined from the Stark broadening of the Si (I) 288.16 nm emission line and were found to be in the range 2.79×10^{16} cm^{-3} to 5.59×10^{19} cm^{-3}. Excitation temperatures of 9000 - 21000 K were calculated using the Si (I) 288.16 nm emission line to continuum ratio. The morphology of the laser plume, observed with respect to time, was seen to be strongly dependent on the ambient pressure. The density and temperature of the plasma was also found to vary critically with plasma morphology. Three ambient pressure regimes were identified where the plasma evolution was observed to differ markedly. Requirements for the existence of local thermal equilibrium conditions in the laser-induced plasmas are discussed with respect to these results.

Keywords:
LIBS, laser ablation plasma diagnostics, vacuum, ambient pressure, silicon, Local Thermal Equilibrium, morphology.

Subject classification numbers (PACS):

52.25.-b	Plasma properties
52.38.Mf	Laser ablation
52.70.Kz	Optical measurements

Submitted to:
Journal of Physics D: Applied Physics

1. Introduction

Laser-Induced Breakdown Spectroscopy (LIBS) is a powerful Optical Emission Spectroscopy (OES) analytical tool capable of sampling solids, liquids and gases for research and industrial applications [1-7]. A pulsed laser source is employed to vaporise and excite an analyte forming a transient plasma or plume which subsequently expands away from the sample surface. The optical emission from the relaxation of excited species within the plasma yields information regarding the composition of the material under test. LIBS historically has been a qualitative technique but over recent years it has developed into a pseudo-quantitative materials micro-analysis technique, capable of determining the elemental composition of solids, liquids and gases [2].

The basis of the LIBS technique requires the formation of a short lived plasma from the sample. High intensity pulsed laser radiation is focussed onto the sample and if the laser fluence exceeds a material specific threshold value, typically $10^9 – 10^{14}$ W m^{-2} [1], then the sample is ablated forming a plume propagating away from the sample surface. The ablated material is composed of neutral particles, free electrons and ionic species, and expands as a high temperature plasma, approximately 10^3 - 10^5 K [1,3,6]. Spectroscopic analysis of the optical emission from the excited plasma species enables identification of the material under test. Typically the optical emission from the expanding plasma is dispersed using a spectrograph and subsequently captured and analysed. The captured emission spectrum provides information regarding the elemental composition of the sample, the temperature and particle density of the plasma, and the degree of plasma fractional ionisation. Suitably delayed gated capture of the emission spectra from laser-induced plasmas enables temporal investigation of plasma characteristics and expansion dynamics [3,7]. Several excellent review articles [2,3,5-9] regarding LIBS fundamentals, applications and experimental approaches have been published.

The versatility of LIBS has seen it employed in numerous industrial [10-13], environmental [14-16] and archaeological [17-19] applications, to give but a few examples.

Spectroscopic analysis of laser-induced plasmas can lead to the determination of electron number densities from the Stark broadening of emission line profiles [20,21]; plasma temperatures may be determined from the 2 line ratio method [20], Boltzmann plot method [22,23] and line-to-continuum ratio method [24,25] Milàn and Laserna [26] performed diagnostics of silicon plasmas produced by nanosecond Nd:YAG 532 nm pulses, in air at atmospheric pressure. Plasma temperatures determined, using the Boltzmann plot method, tended to remain constant with increasing delay and were reported to be in the range of 6000 - 9000 K. This behaviour, contrary to their expectations, was ascribed to difficulties in finding silicon lines fulfilling the requirements of the Boltzmann plot method. Electron densities of the order 10^{18} cm^{-3} were determined from the Stark broadening of the Si (I) 250.65 nm line. Liu et al. [24] performed spectroscopic analyses of silicon plasmas induced by nanosecond Nd:YAG 266 nm pulses, in air at atmospheric pressure. Plasma temperatures were ascertained using the line-to-continuum ratio method and found to be in the range 20000 – 70000 K during the early phase (<300 ns) of plasma expansion. Electron densities of 10^{18} - 10^{19} cm^{-3} were calculated from the Stark broadening of the Si (I) 288.16 nm line.

The electron densities and temperatures reported by Milàn and Laserna [26] and Liu et al. [24] for silicon plasmas are comparable to those calculated for other solid analytes in air at atmospheric pressure. Shaikh et al. reported temperatures in zinc plasmas, using Nd:YAG (532 nm) nanosecond pulses, of approximately 9000 K determined by the 2-line method, and electron densities of the order 10^{16} cm^{-3} [20]. Drogoff et al. report electron densities of the order $10^{16} – 10^{18}$ cm^{-3}, and plasma temperatures in the range 5500 – 11000 K for Nd:YAG (1064 nm) nanosecond pulse laser induced aluminium plasmas [22].

The ambient atmosphere plays an important role in dictating the morphology and evolution of laser-induced plasmas [1,23]. The ambient gas confines the plasma and in some cases may react with it. The observed plasma emission intensity dependence on ambient gas pressure and composition is extremely complex [7]. It is generally recognised that as the ambient pressure decreases the emission intensity and plasma lifetime also decreases due to a lack of external ambient confinement [1,23,27] and that the signal to background ratio is improved due to the reduced continuum radiation at lower plasma densities [28,29]. Laser-induced plasmas may also exhibit increased emission intensity at lower pressures due to lessened plasma shielding, and therefore greater sample ablation [1,3].

Harilal et al. performed electron density and temperature measurements from Nd:YAG (1064 nm) laser induced plasmas at an ambient pressure of ~ 10^{-4} mbar; electron densities of the order 10^{17} cm^{-3} and temperatures in the range 17000 – 40000 K were reported [30]. Radziemski et al. conducted LIBS of geological samples in a simulated Martian atmosphere, and reported that the appearance and characteristics of the induced plasma plumes were strongly pressure dependent [27]. Harilal et al. applied 2 ns gated ICCD photography to characterize the morphology of laser-induced aluminium plumes through a range of ambient pressures from ~ 10^{-6} to 100 mbar [31].

2. Experimental set-up

The apparatus shown in Figure 1 is designed for LIBS material analysis and plasma plume characterisation through a range of ambient pressure regimes, from atmospheric down to a pressure, p_a, < 10^{-6} mbar, [29]. The set-up includes an Nd:YAG laser (Continuum, Surelite), frequency doubled to produce an output at 532 nm, with a 4-6 ns pulse length and a peak power of 200 mJ. For this investigation the laser was operated at a repetition rate of 10 Hz unless otherwise specified. Laser radiation was focussed onto the sample surface using a 150 mm plano-convex quartz lens, with a spot size of ~ 400 µm at the sample. Samples were placed perpendicular to the direction of the laser beam.

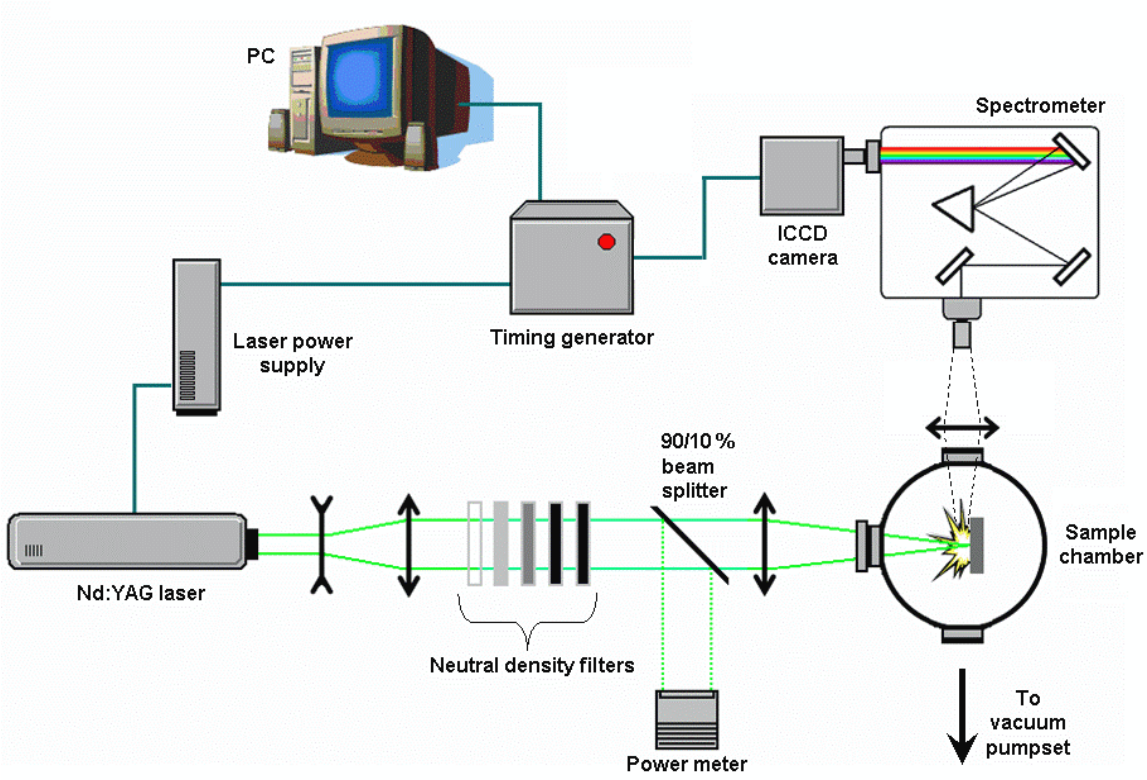

Figure 1. The LIBS apparatus

The material under test was mounted in the vacuum chamber on a rotating stage such that each LIBS analysis could be carried out on a fresh piece of the sample. A turbomolecular and rotary pump set was used to evacuate the chamber to $p_a < 10^{-6}$ mbar. A molecular sieve foreline trap was employed to reduce pump oil contamination.

Optical emission from the plasma plume was collected, at 90° to the direction of laser beam propagation, through a quartz window in the vacuum chamber wall. Plasma plumes were imaged using a plano-convex quartz lens (focal length 100 mm) onto the entrance slit of an Acton Research Spectra Pro 500i 0.5 m imaging triple grating (150, 600, 2400 grooves mm^{-1}) spectrometer. Dispersed images of the plasma were captured with the spectrometer input slit width set to 10 µm, non-dispersed images were captured with a slit width of 3 mm. The spectrometer input slit was orientated to capture images along the entire plume length in the direction of plume propagation; all measurements taken were thus spatially integrated along the length of the plume. The output of the spectrometer was coupled to a Princeton Instruments PI-MAX ICCD camera that utilized a proximity focussed MCP intensifier connected via a fibre-optic coupling to the CCD array; the 1024 × 256 pixel CCD array being thermoelectrically cooled to -20°C. The laser power supply, camera and PC were connected to a Princeton Instruments ST-133A programmable timing generator, enabling temporal resolution of the plasma plume.

Standard semiconductor grade polished silicon [111] wafers were used in this study. Electron temperature and density measurements were performed with the 2400 grooves mm^{-1} grating, using the neutral Silicon (I) 288.16 nm emission line arising from the $3s^2 3p^2 - 3s^2 3p4s$ transition. Non-dispersed images of the plasma were collected with the 2400 grooves mm^{-1} grating positioned to allow the zero order to propagate to the ICCD. Spectral resolution when using the 2400 grooves mm^{-1} grating was 0.02 nm $pixel^{-1}$.

3. Results

3.1 Plasma electron temperature

Use of the Boltzmann plot for plasma temperature determination proved difficult as there were very few, simultaneously produced, suitable Si (I) emission lines within the narrow wavelength range that the LIBS system requires. This problem has been noted previously for silicon by Milàn and Laserna [26]. The excitation temperature was therefore determined using the line-to-continuum ratio method [24, 25], which relies on the accurate measurement of the continuum level. At delay times greater than ~ 2 µs at atmospheric pressure, and greater than ~ 1.4 µs at $p_a \sim 10^{-4}$ mbar, the continuum may no longer be resolved above the dark charge level of the ICCD. As such, this study focussed on temporal evolution of plasma plumes up to a maximum delay of 1410 ns. To employ the line-to-continuum ratio method, a Voigt curve was fitted to each data set, as shown in Figure 2.

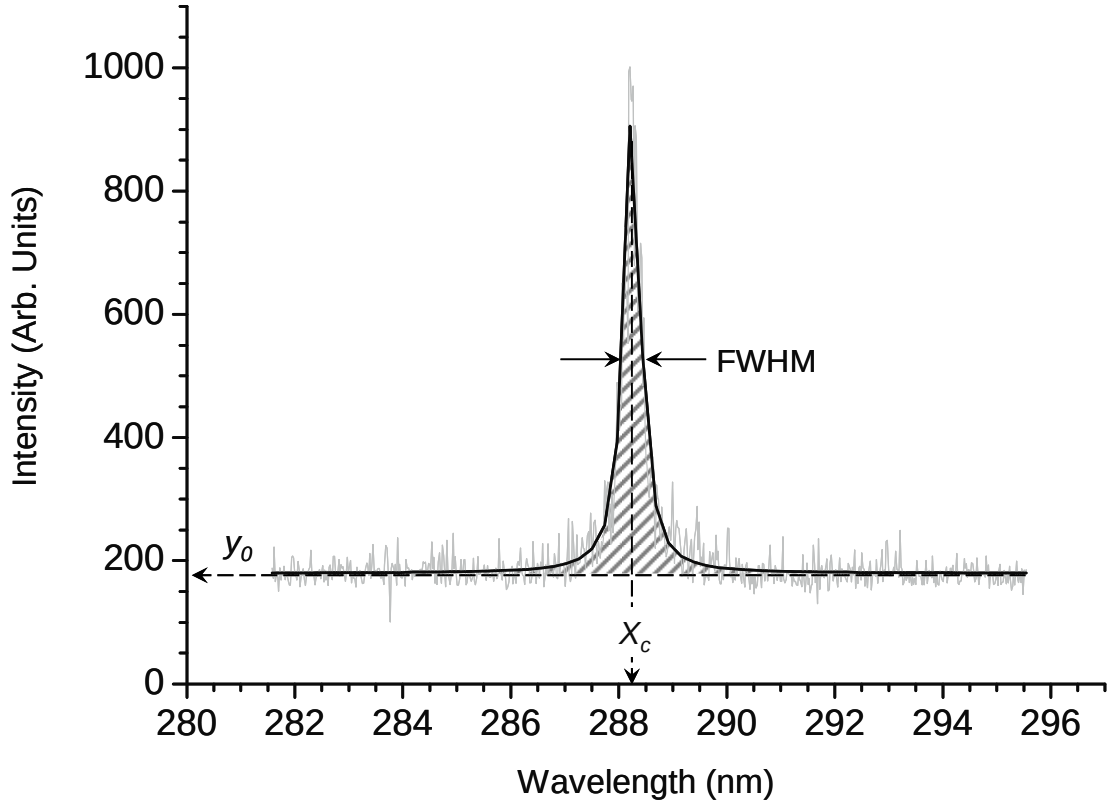

Figure 2. Example of a Voigt curve fitted to the Si (I) 288.16 nm emission line. The captured spectral data is given in grey, the Voigt fit is shown in black. The shaded region represents the integrated area of the curve, *A*. The centre wavelength of the peak is represented by x_c, and the baseline offset by y_0.

All spectra were corrected to account for the spectral response of the instrument, and the ICCD dark charge was subsequently subtracted. Using the parameters resulting from the Voigt fit to the 288.16 nm Si (I) emission line, and assuming Local Thermal Equilibrium (LTE) conditions exist within the plasma, the plasma excitation temperature T_e may be calculated using Equation 1 [24].

$$\frac{\varepsilon_l}{\varepsilon_c}(\lambda) = C_r \frac{A_{21} g_2}{U_i} \frac{\lambda_c^2}{\lambda_l T_e} \frac{\exp\left(\frac{E_i - E_2 - \Delta E_i}{kT_e}\right)}{\left[\xi\left(1 - \exp\frac{-hc}{\lambda kT_e}\right) + G\left(\exp\frac{-hc}{\lambda kT_e}\right)\right]} \qquad (1)$$

where C_r = 2.005 x 10^{-5} (s K), A_{21} is the transition probability, E_i is the ionisation potential, E_2 is the upper state energy level, and g_2 the upper state statistical weight. ΔE_i is the lowering of the ionisation potential of atoms in the presence of a field of ions and is small enough to be deemed insignificant [24]. U_i is the partition function for a silicon ion, and was calculated in the range 5.84 – 6.87 over the temperature conditions of this study. G is the free-free Gaunt factor, which is assumed to be unity [24]. ξ is the free-bound continuum correction factor, and was calculated for Si vapour by Liu et al. as 1.4 [24]. ε_c is the continuum emission coefficient and is equal to y_0 obtained from the Voigt fit. ε_l is the integrated emission coefficient over the line spectral profile, and is given by the integrated area of the fitted Voigt curve, *A*. λ_c and λ_l are the continuum wavelength and line wavelength (nm) respectively; from the Voigt curve fit: $\lambda_c = \lambda_l = x_c$. The parameters used for plasma temperature determinations are summarized in Table 1. There is no simple analytical solution for

Equation 1; as such an iterative process was employed to solve for T_e numerically. The Si^+ partition function is a dependent of temperature and therefore was required to be re-calculated at each successive stage of the iterative solution for T_e. Values of T_e, and hence U_i, were found to converge to steady values after five cycles of this iterative process.

Table 1. Parameters used for plasma temperature determinations [24,32].

Transition (nm)	A_{21} (10^8 s^{-1})	G_2	E_2 (eV)	E_i (eV)	U_i	ξ	G	C_r (sK)
Si (I) 288.16	1.9	3	5.028	8.151	5.84 – 6.87	1.4	1	2.005 x 10^{-5}

The excitation temperature T_e was determined using Equation 1 for delay times of 10 to 1410 ns, over a range of 8 pressures from atmospheric to 1 × 10^{-4} mbar; these data are plotted in Figure 3.

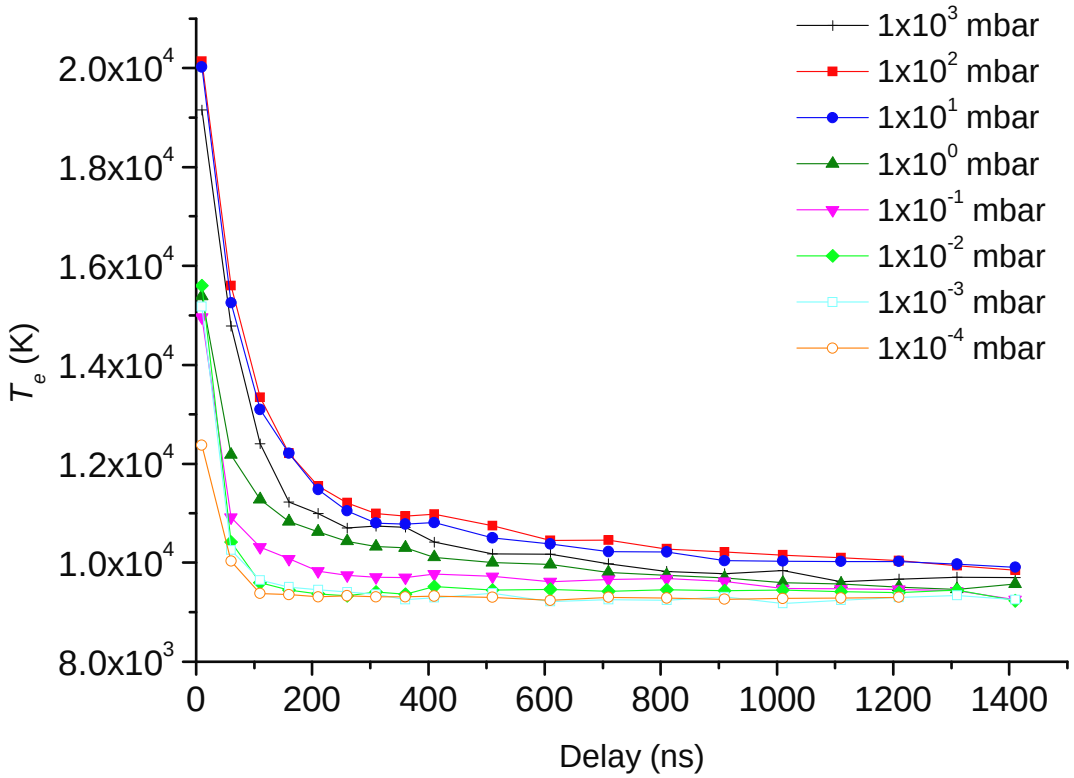

Figure 3. Plasma excitation temperature T_e versus capture delay time, for ambient pressures in the range 1 × 10^3 to 1 × 10^{-4} mbar.

It can be seen from Figure 3 that the maximum determined T_e are evident at p_a of 100 and 10 mbar; below 10 mbar there is a general decrease in plasma temperature with decreasing ambient pressure. The maximum calculated excitation temperature T_e here was 21000 K, the minimum was 9100 K. At each ambient pressure considered, the decrease of plasma temperature with time was found to best fit a second order exponential decay; the coefficient of determination R^2 for each fit is listed in Table 2.

Table 2. Coefficients of determination, R^2, for a second order exponential decay as fitted to the excitation temperature data presented in Figure 3

Pressure (mbar)	R^2	Pressure (mbar)	R^2
1×10^{3}	0.99723	1×10^{-1}	0.99570
1×10^{2}	0.99915	1×10^{-2}	0.99825
1×10^{1}	0.99951	1×10^{-3}	0.99885
1×10^{0}	0.99914	1×10^{-4}	0.99722

3.2 Plasma electron density

The electron density of the laser ablation plasma was determined from the Stark broadening of the 288.16 nm Si (I) emission line. The contributions of resonance and Doppler line broadening were deemed insignificant under the conditions of this study. Resonance broadening is negligible as the 288.16 nm Si (I) line is not associated with a ground state [24, 33]. The Doppler effect will cause a broadening in line width for Si (I) 288.16 nm of less than 0.0055 nm, assuming that the plasma temperature is the maximum determined in this study. This value was estimated using Equation 2 [24].

$$w_{1/2} = 7.19 \times 10^{-10} \lambda \, (T/M)^{1/2} \qquad (2)$$

Where $w_{1/2}$ is the Doppler broadening contribution in nm, λ is the line wavelength in nm, T is the plasma temperature in Kelvin, and M is the atomic mass expressed in amu. The electron density of the plasma is related to the Stark pressure broadening of the emission lines by Equation 3 [26].

$$\Delta\lambda_{1/2} = 2w\left(\frac{N_e}{10^{16}}\right) + 3.5A\left(\frac{N_e}{10^{16}}\right)^{1/4}\left[1 - 1.2N_D^{-1/3}\right]w\left(\frac{N_e}{10^{16}}\right) \qquad (3)$$

where $\Delta\lambda_{1/2}$ is the FWHM broadening of the line, N_e is the plasma electron number density, w and A are the electron impact width parameter and the ion broadening parameter respectively, and N_D is the number density of particles in the Debye sphere, given by Equation 4 [26],

$$N_D = 1.72 \times 10^{9} \frac{T^{3/2}}{N_e^{1/2}} \qquad (4)$$

Where T is the plasma temperature. Due to the small ionic contribution to Stark broadening, Equation 4 may be simplified to Equation 5 [20,26].

$$\Delta\lambda_{1/2} = 2w\left(\frac{N_e}{10^{16}}\right) \qquad (5)$$

The electron impact broadening width parameter w is temperature dependent, and was interpolated for each appropriate temperature from the values given by Griem [34]. The observed line profile is a convolution of the Stark broadening of the emission lines and the broadening contribution of the instrument. The instrument broadening contributes a Gaussian component to the observed line shape, the Stark effect a Lorentzian contribution to the observed line profile. A deconvolution of the Voigt fit to each spectrum was performed, with the Gaussian FWHM fixed as the instrumental broadening contribution; in this way the FWHM of the emission lines was determined. The instrumental broadening profile was found to be 0.04 nm, measured using several narrow emission lines from a cadmium hollow cathode lamp.

The plasma electron density was calculated using Equation 5 for delay times of 10 to 1410 ns, over a range of 8 pressures from atmospheric to 1×10^{-4} mbar; these data are plotted in Figure 4.

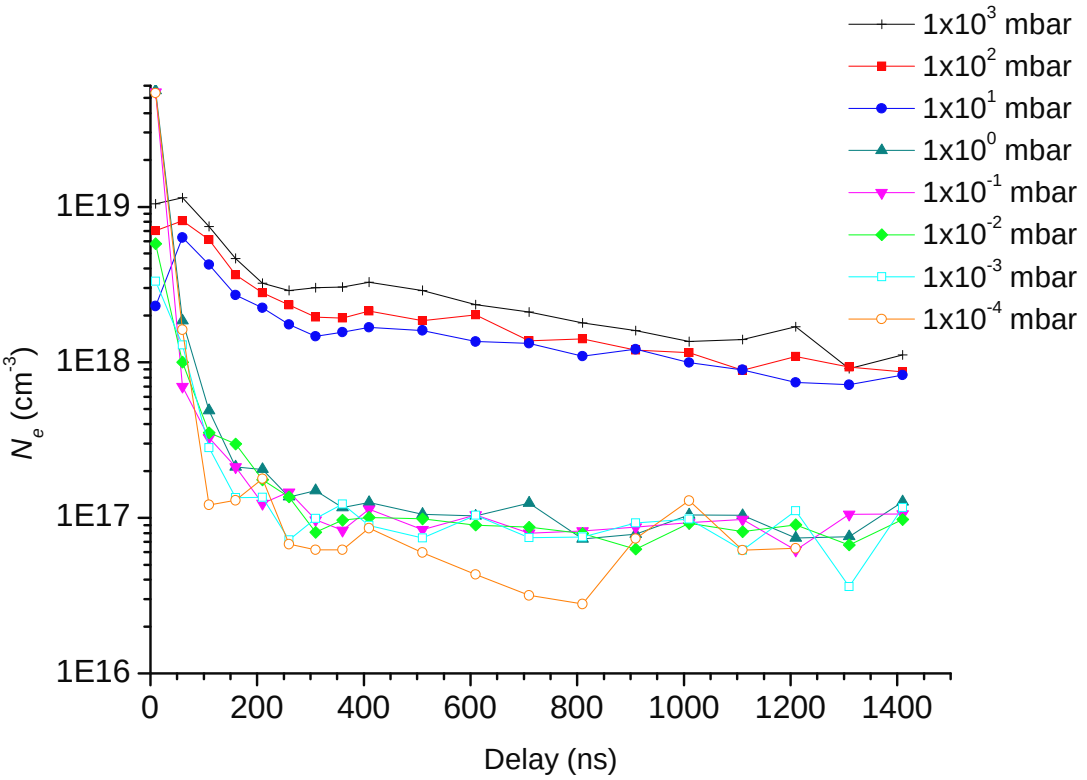

Figure 4. Plasma electron density N_e versus capture delay time, for ambient pressures in the range 1×10^3 to 1×10^{-4} mbar.

Figure 4 reveals that there is a general decrease in plasma electron density with ambient pressure. The most striking feature of Figure 4 is the step change in the plasma behaviour, between ambient pressures of ≥ 10 mbar and ≤ 1 mbar. The decrease in the plasma electron density with increased delay times was found to fit a second-order exponential decay. The coefficients of determination R^2 for each fit are listed in Table 3; such fits describe the captured data more accurately at ambient pressures below 1 mbar.

Table 3. Coefficients of determination, R^2, for second-order exponential fits to the electron number density data presented in Figure 4

Pressure (mbar)	R^2	Pressure (mbar)	R^2
1×10^3	0.92206	1×10^{-1}	0.99998
1×10^2	0.91586	1×10^{-2}	0.99839
1×10^1	0.92732	1×10^{-3}	0.99493
1×10^0	0.99994	1×10^{-4}	0.99941

The maximum recorded electron number density was found to be 5.59×10^{19} cm^{-3}, and the minimum 2.79×10^{16} cm^{-3}.

3.3 Local Thermal Equilibrium considerations

For any given plasma to be considered to be in LTE the lower limit for the electron number density N_e must satisfy Equation 6 [26,33]:

$$N_e \ (\text{cm}^{-3}) \geq 1.6 \times 10^{12} \ T^{1/2} \ \Delta E^{3} \qquad (6)$$

Where ΔE (eV) is the energy difference between the upper and lower states and T (K) is the plasma temperature. For the Si (I) 288.16 nm line transition, ΔE = 4.3 eV. Considering the highest plasma temperature measured here, $T_e \sim 2.1 \times 10^4$ K, yields a minimum electron density of $N_e \geq 1.81 \times 10^{16}$ (cm^{-3}). It is apparent that, throughout the parameter space of this study, N_e is greater than the limit defined in Equation 6. It should be noted, however, that N_e is only just greater than this limit at lower ambient pressures, and hence the assumption that LTE exists must be treated with caution. It should also be noted that the criterion outlined in Equation 6 is a necessary, but not the only, requirement for LTE.

3.4 Plasma morphology

Figures 5a to 5h show time-resolved non-dispersed images of the laser–induced silicon plasmas from atmospheric pressure down to $p_a \sim 10^{-4}$ mbar. The laser was operated in single shot mode with each shot on a clean area of the sample; the intensity scale of each image was normalized to its maximum intensity. The direction of laser propagation was from the top of each image to the bottom, with the sample surface lying perpendicular to the laser beam and the plasma being generated vertically upwards. All indicated capture delay times are given in ns.

In order to prevent ICCD spot damage from intense plasma emission, a ND 1.2 neutral density filter was placed in front of the spectrometer input slit. The integration time for each capture was 1 ns, and the intensifier gain was set to 200. The plumes appeared asymmetrical about the axis of the laser beam propagation due to irregularities in the beam profile. It can be seen that in the early stages of plasma formation, ~ 110 ns, the plasmas generated at each ambient pressure are comparable in terms of size and luminosity. This similarity is backed up by the spectroscopic measurements of N_e and T_e. The plasma disperses much more rapidly under lower ambient pressure due to free plasma expansion on account of an increased mean free path of the confining ambient gas; this is again supported by the spectroscopic measurements of N_e and T_e.

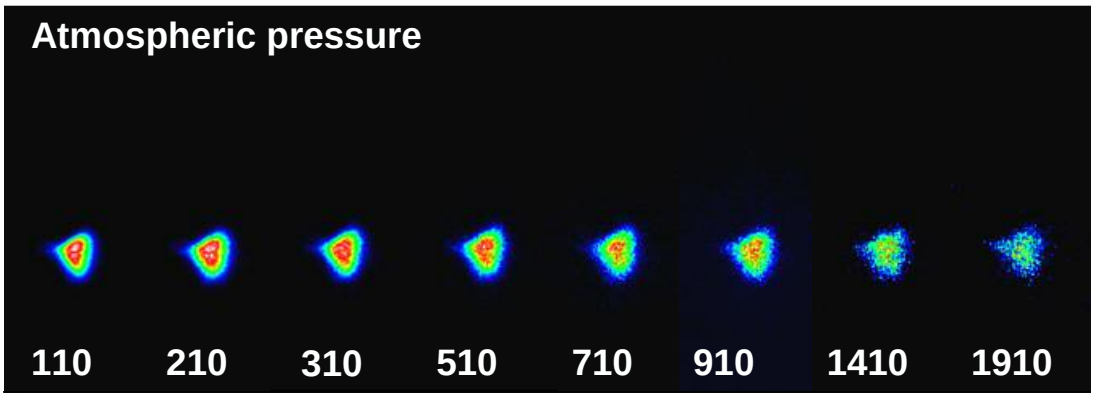

Figure 5a. Plasma morphology at atmospheric pressure versus capture delay time (ns)

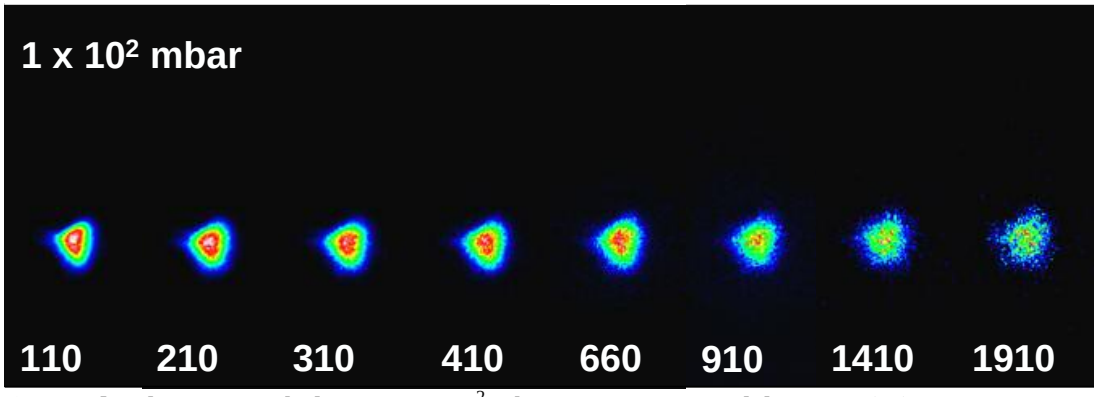

Figure 5b. Plasma morphology at 1 x 10^2 mbar versus capture delay time (ns)

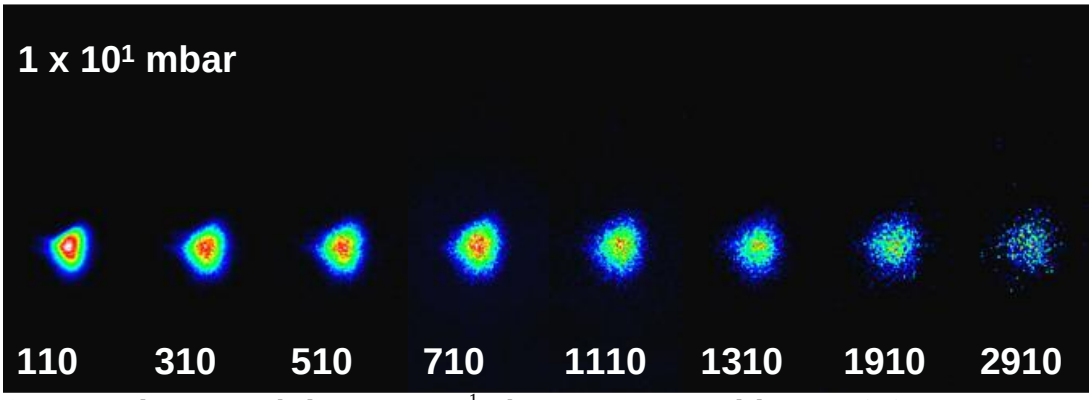

Figure 5c. Plasma morphology at 1 x 10^{1} mbar versus capture delay time (ns)

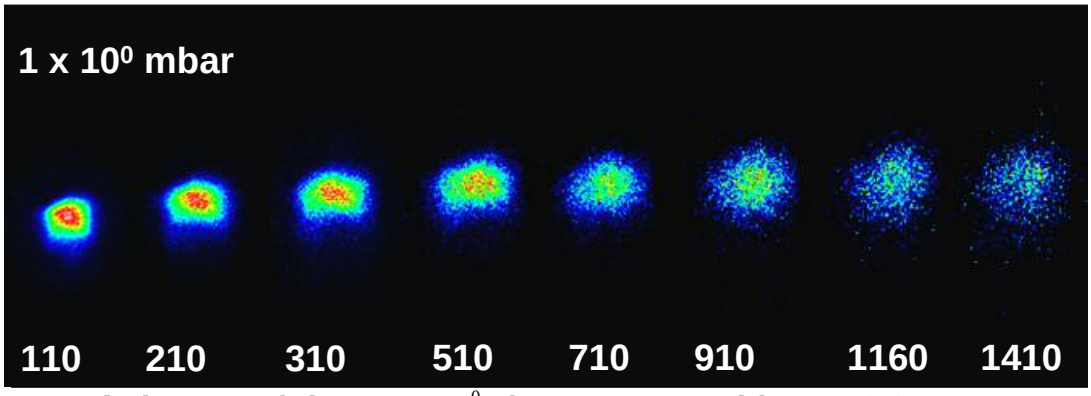

Figure 5d. Plasma morphology at 1 x 10^{0} mbar versus capture delay time (ns)

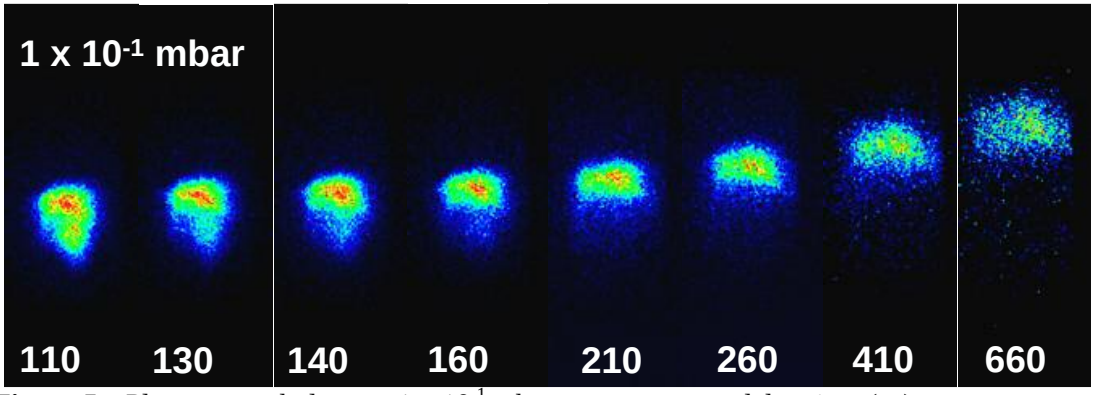

Figure 5e. Plasma morphology at 1 x 10^{-1} mbar versus capture delay time (ns)

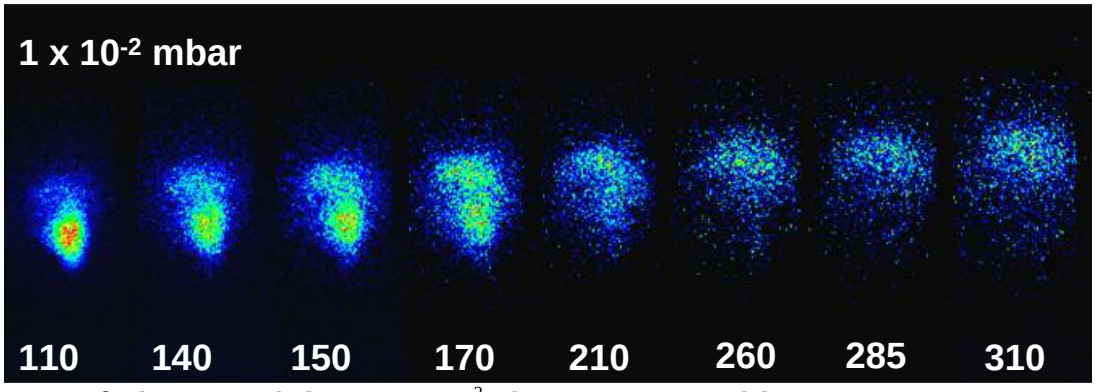

Figure 5f. Plasma morphology at 1 x 10^{-2} mbar versus capture delay time (ns)

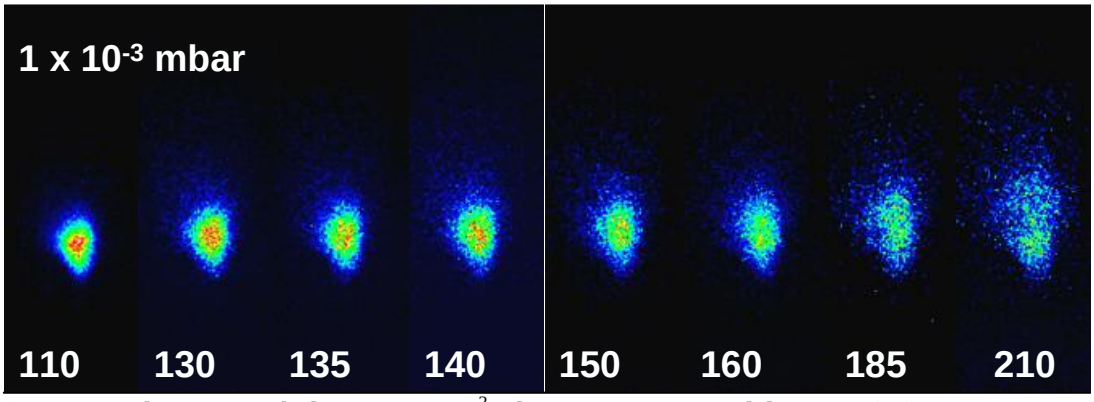

Figure 5g. Plasma morphology at 1 x 10^{-3} mbar versus capture delay time (ns)

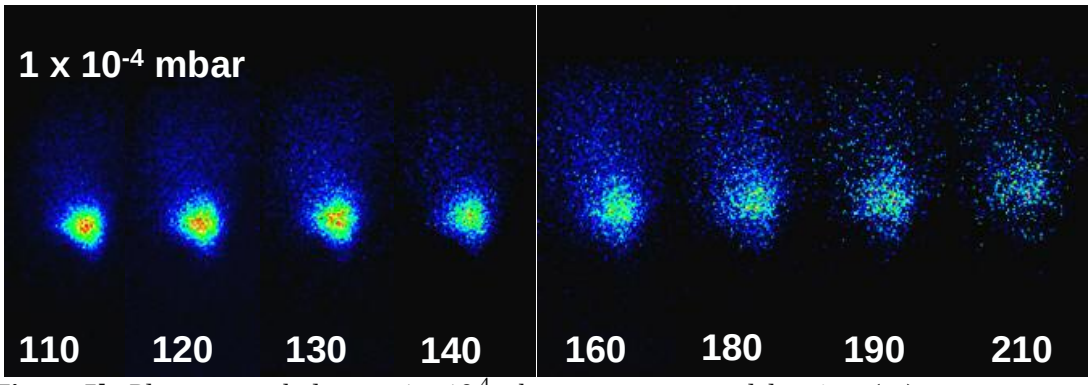

Figure 5h. Plasma morphology at 1 x 10^{-4} mbar versus capture delay time (ns)

At atmospheric pressure, 1×10^{2} and 1×10^{1} mbar there is little discernible difference in the shape, size, luminosity or lifetime of the laser induced silicon plasmas. In Figure 5d, at an ambient pressure of 1×10^{0} mbar the plasma is seen to leave the sample surface as it expands, a trend continued at ambient pressures of 1×10^{-1} and 1×10^{-2} mbar, shown in Figures 5e and 5f.

At ambient pressures of 1×10^{-3} mbar and below, shown in Figures 5g and 5h, the plasma does not leave the sample surface as it expands. Figures 5a through to 5h indicate that, below an ambient pressure of 1×10^{1} mbar, further pressure decreases reveal an expected acceleration in the rate of plasma expansion.

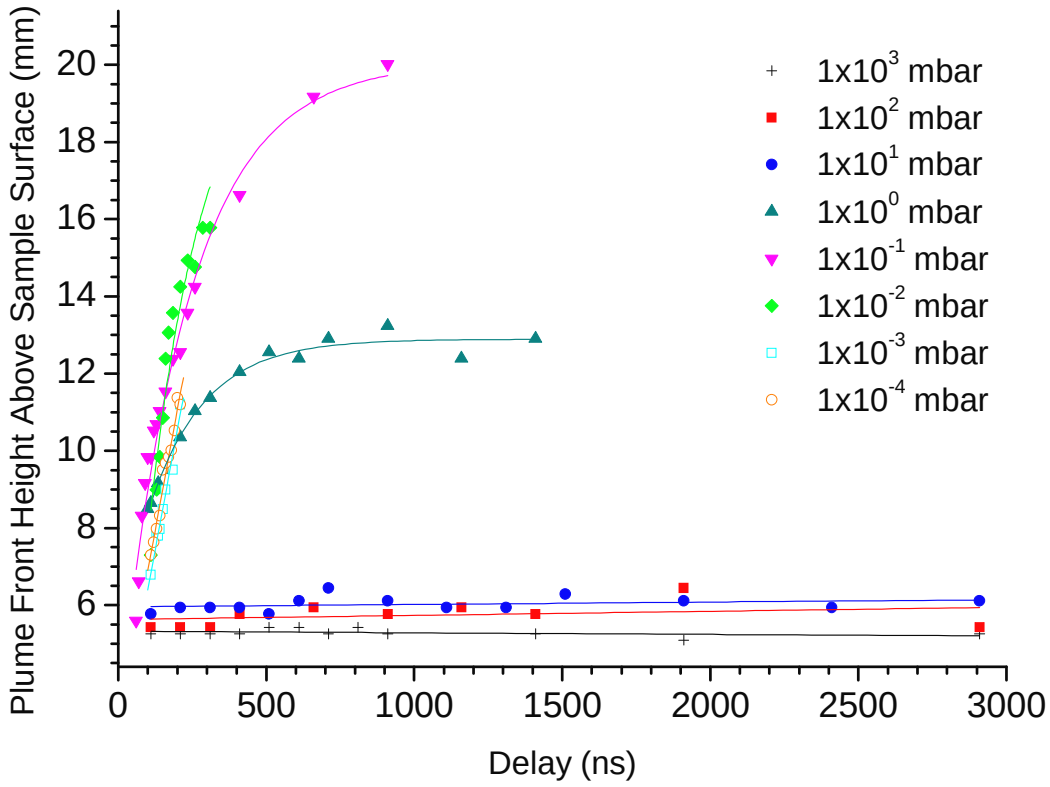

Figure 6. Plasma plume front height position above sample surface versus capture delay time, for ambient pressures in the range 1×10^{3} to 1×10^{-4} mbar.

Figure 6, a plot of the plasma plume front height above the sample surface versus delay time, indicates plume confinement at pressures of 1×10^{1} mbar and above, with the plasma remaining virtually the same length throughout the observation period. At ambient pressures of 1×10^{0} and 1×10^{-1} mbar the plasma plume front propagates away from the sample surface, but the traces for these pressures indicate a deceleration of the plume front, and by inference a degree of plasma confinement. At ambient pressures $\leq 1 \times 10^{-2}$ mbar the plume front moves away from the sample surface with a constant velocity, indicating free plasma expansion and little plume confinement.

4. Discussion

Two distinct groups of data can be seen, one representing the plasmas that are confined to the substrate surface by the ambient gas pressure, the other representing plasmas that have detached from the silicon substrate surface and are thus undergoing free expansion. The evaluation of the plasma excitation temperature at atmospheric pressure, using the line-to-continuum ratio method, produced results that were in good agreement with the published data [20,22,24,26]. It is shown that as the ambient pressure decreases the excitation temperature and electron number density decrease, which is to be expected. The maximum calculated excitation temperatures were observed at ambient pressures of 1×10^{2} and 1×10^{1} mbar; the pressure region through which the plasma is confined to the substrate surface.

The electron number density behaviour appears to be separated into two ambient pressure dependent regimes. For ambient pressures $\geq 1 \times 10^{1}$ mbar the electron number density decreases steadily from ~ 10^{19} to ~ 10^{18} cm^{-3} over 1400 ns. For ambient pressures $< 1 \times 10^{1}$ mbar there is a sudden drop in electron number density from ~ 10^{19} to ~ 10^{17} cm^{-3} in the first 200 ns of plume evolution, followed by a much slower decrease over the remainder of the observation period.

The highest electron number densities are observed at atmospheric pressure, and drop with decreasing ambient pressure. The step change in electron number density is evident, dropping by approximately an order of magnitude between ambient pressures of 10 and 1 mbar.

It is postulated that the spectroscopic measurements obtained throughout this work are dependent on the plasma morphology, which in turn is seen broadly to depend on the ambient pressure. At the initial point of plasma formation, and during the first few nanoseconds of plasma lifetime, the ambient pressure plays little part in dictating the shape, size and properties of the plasma, as seen in Figures 5a to 5h and confirmed by the spectroscopic measurements. As the plasma front subsequently expands into the ambient gas, the ambient pressure now begins to affect these properties, with differing plasma expansion dynamics observed at different ambient pressures.

By extrapolation it is seen that the mean free path relating to this pressure boundary possesses a value that is of the order of the plume dimensions. It is therefore concluded that, as a simplistic first approximation, the plasma expansion dynamics change at the point where the mean free path of the confining ambient gas approaches the dimensions of the plasma. This observation can now help to explain the three observed pressure-dependent plasma behaviour regions:

1. where the mean free path of the ambient gas is small compared to the plasma dimensions, the plasma is confined
2. where the mean free path of the ambient gas is large compared to the plasma dimensions, free expansion of the plasma is observed
3. at intermediate ambient pressures a 'transition region' exists wherein there is a degree of plasma confinement, but the plasma is observed to propagate slowly away from the substrate surface.

The above discussion of the plasma expansion dynamics is, of course, a highly simplified description. It is known that laser-induced plasma formation and expansion is a complex process [1,2,7]. This preliminary investigation into the pressure dependence of laser-induced plasma expansion neglects the influences of shockwave formation and propagation, plasma shielding and ablation rates, and reactions between the ambient gas and plasma etc. Further investigation will be required to fully describe and characterise the plasma formation and evolution processes.

5. Conclusion

Laser-Induced Breakdown Spectroscopy of silicon was performed using a nanosecond pulsed frequency doubled Nd:YAG (532 nm) laser. The temporal evolution of the laser ablation plumes through a range of ambient pressures was characterized in terms of temperature, electron number density and plasma morphology. Excitation temperatures were obtained from the Si (I) 288.16 nm emission line to continuum ratio, and were found to be in the range 9100 - 21000 K. Plasma temperature was found to decrease with time following a second-order exponential decay at each pressure considered here. This decrease hints at a two-phase plasma expansion, with an initial rapid drop in temperature followed by a slow, steady temperature decay over time. In general, there was seen to be a decrease in plasma temperature with respect to ambient pressure, with maximum plasma temperatures recorded at ambient pressures of 1×10^2 and 1×10^1 mbar.

Electron densities were determined from the Stark broadening of the Si (I) 288.16 nm emission line, in the range 2.79×10^{16} cm^{-3} to 5.59×10^{19} cm^{-3}. At each ambient pressure considered, the plasma electron number density was observed to fulfil the criterion for LTE as outlined in Equation 6. A decrease in plasma electron density with respect to ambient pressure, with a step-change in plasma expansion dynamics was observed between pressures

of 1×10^1 and 1×10^0 mbar. The density and temperature of the plasma was found to vary critically with plasma morphology, which is in turn was strongly dependent on ambient pressure. These preliminary conclusions were justified by comparison of the plasma dimensions to the mean free path of the ambient gas. Further work will be required to fully characterise the laser-induced plasma formation and expansion process.

6. References

[1] Cremers D.A., Radziemski L.J., *'Handbook of laser-induced breakdown spectroscopy'* John Wiley and Sons Ltd, Chichester, 2006. ISBN 13 978-0-470-09299-6.

[2] Vadillo J.M., Laserna J.J. *'Laser-induced plasma spectrometry: truly a surface analytical tool'* Spectrochimica Acta Part B (2004) 59, 147-161.

[3] Amoruso S., Bruzzese R., Spinelli N., Velotta R. *'Characterization of laser-ablation plasmas'* Journal of Physics B: At. Mol. Opt. Phys. (1999) 32, R131-R172.

[4] Yueh F., Singh J.P., Zhang H. *'Laser-Induced Breakdown Spectroscopy, Elemental Analysis'* in Meyers R.A. (Ed.) Encyclopedia of Analytical Chemistry pp. 2066-87. John Wiley & Son Ltd., Chichester (2000).

[5] Russo R.E., Mao X.L., Liu C., Gonzalez J. *'Laser assisted plasma spectrochemistry: laser ablation'* Journal of Analytical Atomic Spectrometry (2004) 19, 1084-1089.

[6] Rusak D.A., Castle B.C., Smith B.W., Winefordner J.D. *'Recent trends and the future of laser-induced plasma spectroscopy'* Trends in Analytical Chemistry (1998) 17, 453-461.

[7] Tognoni E., Palleschi V., Corsi M., Cristoforetti G. *'Quantitative micro-analysis by laser-induced breakdown spectroscopy: a review of the experimental approaches'* Spectrochimica Acta Part B (2002) 57, 1115-1130.

[8] Radziemski L.J. *'From LASER to LIBS, the path of technology development'* Spectrochimica Acta Part B (2002) 57, 1109-1113.

[9] Sallé B., Mauchien P., Maurice S. *'Laser-Induced Breakdown Spectroscopy in open-path configuration for the analysis of distant objects'* Spectrochimica Acta Part B (2007) 62, 739-768.

[10] Noll R., Mönch I., Klein O., Lamott A. *'Concept and operating performance of inspection machines for industrial use based on laser-induced breakdown spectroscopy'* Spectrochimica Acta Part B (2005) 60, 1070-1075.

[11] Noll R., Bette H., Brysch A., Kraushaar M., Mönch I., Peter L., Sturm V. *'Laser-induced breakdown spectrometry - applications for production control and quality assurance in the steel industry'* Spectrochimica Acta Part B (2001) 56, 637-649.

[12] Barrette L., Turmel S. *'On-line iron-ore slurry monitoring for real-time process control of pellet making processes using laser-induced breakdown spectroscopy: graphitic vs. total carbon detection'* Spectrochimica Acta Part B (2001) 56, 715-723.

[13] St-Onge L., Kwong E., Sabsabi M., Vadas E.B. *'Rapid analysis of liquid formulations containing sodium chloride using laser-induced breakdown spectroscopy'* Journal of Pharmaceutical and Biomedical Analysis (2004) 36, 277-284.

[14] Harmon R.S., De Lucia F.C., Miziolek A.W., McNesby K.L., Walters R.A., French P.D. *'Laser-induced breakdown spectroscopy (LIBS) – an emerging field-portable sensor technology for real-time, in-situ geochemical and environmental analysis'* Applied Geochemsistry (2006) 21, 730-747.

[15] Rai N.K., Rai A.K. *'LIBS -An Efficient Approach for the Determination of Cr in industrial wastewater'* Journal of Hazardous Materials (2008) 150, 835-838.

[16] Gondal M.A., Hussain T. *'Determination of poisonous metals in wastewater collected from paint manufacturing plant using laser-induced breakdown spectroscopy'* Talanta (2007) 71, 73-80.

[17] Kaminska A., Sawczak M., Komar K., Śliwiński G. *'Application of the laser ablation for conservation of historical paper documents'* Applied Surface Science (2007) 253, 7860-7864.

[18] Brysbaert A., Melessanaki K., Anglos D. *'Pigment analysis in Bronze Age Aegean and Eastern Mediterranean painted plaster by laser-induced breakdown spectroscopy (LIBS)'* Journal of Archaeological Science (2006) 33, 1095-1104.

[19] Fortes F.J., Cortés M., Simón M.D., Cabalín L.M., Laserna J.J. *'Chronocultural sorting of archaeological bronze objects using laser-induced breakdown spectrometry'* Analytica Chimica Acta (2005) 554, 136-143.

[20] Shaikh N.M., Rashid B., Hafeez S., Jamil Y., Baig M.A. *'Measurement of electron density and temperature of a laser-induced zinc plasma'* Journal of Physics D: Applied Physics (2006) 39, 1384-1391.

[21] El Sherbini A.M., Hegazy H., El Sherbini Th.M. *'Measurement of electron density utilizing the H_α-line from laser produced plasma in air'* Spectrochimica Acta Part B (2006) 61, 532-539.

[22] Le Drogoff B., Margot J., Chaker M., Sabsabi M., Barthélemy O., Johnston T. W., Laville S., Vidal F., von Kaenel Y. *'Temporal characterization of femtosecond laser pulses induced plasma for spectrochemical analysis of aluminum alloys'* Spectrochimica Acta Part B (2001) 56, 987-1002.

[23] Lee Y., Song K., Sneddon J. *'Laser Induced Plasmas for Analytical Spectroscopy'* in: Sneddon J., Thiem T.L., Lee Y. (Eds.), Lasers in Analytical Atomic Spectroscopy, VCH publishers Inc., New York, 1997, pp. 197-236.

[24] Liu H.C., Mao X.L., Yoo J.H., Russo R.E. *'Early phase laser induced plasma diagnostics and mass removal during single-pulse laser ablation of silicon'* Spectrochimica Acta Part B (1999) 54, 1607-1624.

[25] Griem H.R., *'Principles of Plasma Spectroscopy'* Cambridge Monographs on Plasma Physics 2, Cambridge University Press, 1997. ISBN 0-521-45504-9.

[26] Milán M., Laserna J.J. *'Diagnostics of silicon plasmas produced by visible nanosecond laser ablation'* Spectrochimica Acta Part B (2001) 56, 275-288.

[27] Radziemski L., Cremers D.A., Benelli K., Khoo C., Harris R.D. *'Use of the vacuum ultraviolet spectral region for laser-induced breakdown spectroscopy-based Martian geology and exploration'* Spectrochimica Acta Part B (2005) 60, 237-248.

[28] Garcia C.C, Vadillo J.M., Palanco S., Ruiz J., Laserna J.J. *'Comparative analysis of layered materials using laser-induced plasma spectrometry and laser-ionization time-of-flight mass spectrometry'* Spectrochimica Acta Part B (2001) 56, 923-931.

[29] Cowpe J.S., Astin J.S., Pilkington R.D., Hill A.E. *'Application of Response Surface Methodology to laser-induced breakdown spectroscopy: Influences of hardware configuration'* Spectrochimica Acta Part B (2007) 62, 1335-1342.

[30] Harilal S.S., Bindhu C.V., Isaac R.C., Nampoori P.N., Vallabhan C.P.G. *'Electron density and temperature measurements in a laser produced carbon plasma'* Journal of Applied Physics (1997) 82, 2140-2146.

[31] Harilal S.S, Bhindu C.V., Tillack M.S., Najmabadi F., Gaeris A.C. *'Internal structure and expansion dynamics of laser ablation plumes into ambient gases'* Journal of Applied Physics (2003) 93, 2380-2388.

[32] CRC Handbook of Chemistry and Physics, CRC Press Inc., Florida, 1988.

[33] Thorne A.P., *'Spectrophysics'* Chapman and Hall Science Paperbacks, London 1974. ISBN 0 412 12510 X, 354-357.

[34] Griem H.R., *'Plasma Spectroscopy'* McGraw-Hill Inc., New York, 1964, Library of Congress Catalog [sic] Card Number 63-23250.